FULL RESEARCH ARTICLE

High- and low-cycle-fatigue properties of additively manufactured Inconel 625

Franco Concli[1] · Riccardo Gerosa[2] · Davide Panzeri[2] · Lorenzo Fraccaroli[1]

Abstract

In the last years, additive manufacturing has become a widespread technology which enables lightweight-design based on topological optimization. Therefore, generation of lattice structures with complex geometries and small thicknesses is allowed. However, a complete metallurgical and mechanical characterization of these materials is crucial for their effective adoption as alternative to conventionally manufactured alloys. Industrial applications require good corrosion resistance and mechanical strength to provide sufficient reliability and structural integrity. Particularly, fatigue behavior becomes a crucial factor since presence of poor surface finishing can decrease fatigue limits significantly. In this work, both the low-cycle-fatigue and high-cycle-fatigue behaviors of Inconel 625, manufactured by Selective Laser Melting, were investigated. Fatigue samples were designed to characterize small parts and tested in the as-built condition since reticular structures are usually adopted without any finishing operation. Microstructural features were studied by light-optical microscopy and scanning-electron microscopy. Finally, fatigue failures were deeply investigated considering fracture mechanics principles with the Kitagawa–Takahashi diagram.

Keywords Selective Laser Melting · High cycle fatigue · Low cycle fatigue · Inconel 625 · Defects · Fractography

Abbreviations

AM	Additive Manufacturing
FCC	Face-Centered Cubic
SLM	Selective Laser Melting
BCT	Body-Centered Tetragonal
TCP	Topologically Close Packed
UTS	Ultimate Tensile Strength
YS	Yield Strength
LOM	Light Optical Microscope
SEM	Scanning Electron Microscope
BR	Build Rate
K-T	Kitagawa–Takahashi
QS	Quasi Static
HCF	High Cycle Fatigue
LCF	Low Cycle Fatigue
EDS	Energy-Dispersive Spectroscopy
PM	Permanent Mold
HPVD	High-Pressure Vacuum Die
RO	Ramberg–Osgood
BCM	Basquin-Coffin-Manson
HIP	Hot Isostatic Pressing

List of symbols

γ'	FCC phase in nickel alloys
γ''	BCT phase in nickel alloys
R	Fatigue load ratio
P	Defect perimeter
A	Defect area
R_a	Surface roughness parameter
R_t	Surface roughness parameter
R_z	Surface roughness parameter
R_c	Surface roughness parameter
R_v	Surface roughness parameter
d	Defect size
e	Surface distance of the defect
HV	Vickers Hardness

✉ Davide Panzeri
davide.panzeri@polimi.it

Franco Concli
franco.concli@unibz.it

Riccardo Gerosa
riccardo.gerosa@polimi.it

Lorenzo Fraccaroli
lorenzo.fraccaroli@unibz.it

1 Faculty of Science and Technology, Free Universiy of Bolzano, Bozen, 39100 Bolzano, Italy

2 Dipartimento Di Meccanica, Politecnico Di Milano, Via La Masa 1, 20156 Milan, Italy

HRB	Rockwell B Hardness
ΔF	Force increment
$\Delta\sigma$	Stress interval
Δa	Crack extension
F_i	Stair-case force level
k	Dixon factor
x_F	Stress level of the last stair-case test
K	Stress Intensity Factor
$\sqrt{\text{area}}$	Defect size parameter (equivalent micro-notch length)
t	Defect depth
ΔK_{th}	Threshold stress-intensity range
$\Delta\sigma_f$	Fatigue limit
α	Constant
σ	Applied stress
Y	Constant
a_0	Intrinsic El-Haddad crack length
$\Delta K_{th,LC}$	Threshold ΔK for long cracks
$\Delta K_{th,eff}$	Intrinsic (effective) ΔK threshold
h	Burgers vector component
k	Burgers vector component
l	Burgers vector component
E	Elastic modulus
b	Burgers vector
a	Edge length of the unit cell
$\Delta\sigma_{th}$	Threshold fatigue stress range
a'_o	Modified a_0 parameter
a^*	Additional parameter
ρ	Density
σ_f	Fatigue limit (50% failure probability)
a	Crack length
σ_{f0}	Theoretical fatigue limit
ε_a	Total strain amplitude
ε_{ae}	Elastic portion of the total strain amplitude
ε_{ap}	Plastic portion of the total strain amplitude
σ_a	Stress amplitude
K	Material constant
n	Material constant
N_f	Number of cycles at failure
ε'_f	Fatigue ductility coefficient
σ'_f	Fatigue strength coefficient
$2N_f$	Number of reversals to failure
b	Fatigue strength exponent
c	Fatigue ductility exponent

1 Introduction

This research project aims at providing reliable data about AM materials to support designers in substituting conventionally manufactured alloys with additively produced ones.

Starting from a virtual 3D CAD model, the SLM technique allows to print layer by layer 3D components with build direction perpendicular to the base plate of the machine. Once the process parameters are defined, the first thin powder layer is uniformly distributed on the base plate. A laser beam is adopted to selectively melt the powder based on the selected scan strategy. Once the first layer is scanned, the base plate is lowered and this stacking process is repeated again until the last layer. During the whole process, an inert gas (argon or nitrogen) is fed into the chamber to avoid reaction of the molten metal especially with oxygen [1].

Thanks to the presence of relatively high contents of Cr, Mo and Nb, Inconel 625 is characterized by an excellent combination of mechanical strength, fatigue properties and corrosion resistance under aggressive conditions. This outstanding behavior is required in several industrial fields, such as aerospace, chemical, oil and gas extraction, power generation and automotive [2–4]. Inconel 625 is often employed in harsh environments involving high temperatures and corrosive media so critical that other materials would fail quickly. In the first case, the creep phenomenon becomes more and more important as the service temperature increases. Moreover, at high temperatures, simple oxidation becomes a significant corrosion mechanism. When fatigue loading, creep and corrosion operate together, the component life can be strongly reduced and it cannot be predicted easily because of the non-linearity introduced by creep and corrosion phenomena. Nevertheless, an estimation of the service life can be done with sufficient reliability assuming that creep, corrosion and fatigue damage mechanisms are independent. Under this hypothesis, they can be related by the linear damage accumulation approach described in the literature [5–7].

AM Inconel 625 has an austenitic matrix with face-centered cubic (FCC) lattice, but a large variety of intermetallic phases and carbides can be precipitated upon sufficient thermal exposure during processing and heat treatment, if any. In fact, the layer stacking process in SLM determines complex thermal cycles in the regions already solidified. Qin et al. [8] observed formation of γ' phase (FCC lattice), γ'' phase (BCT lattice), TCP Laves phases and Cr, Nb and Mo carbides. Additionally, presence of orthorhombic Ni_3Nb phase was observed in the form of inter-dendritic precipitates [9]. Formation of precipitates can deeply alter mechanical properties and corrosion resistance [10, 11]. In fact, carbides and intermetallic phases can determine sensitization of the alloy, because they deplete alloying elements, like chromium and molybdenum, from the surroundings leading to local reductions in the corrosion resistance [10–14]. However, formation of intermetallic phases can provide a hardening effect with an improvement of the mechanical strength at the expense of ductility [10, 11, 14].

In the last years, additive manufacturing has become a spreading technology with more and more materials which

are now available on the market. The major advantages of this technique are the possibility to enable light-weight design of components and generation of complex lattice structures. In this case, topology optimization algorithms can be exploited at the design stage to improve the lattice geometry aiming at optimizing their mechanical performance. For instance, Yang et al. [15] compared three different types of BCC lattice structures to assess the impact of the structural optimization of fillets on the fatigue strength. Rounded fillets generated by topology optimization allowed an improved fatigue performance of the lattice component because of the reduced stress concentration [15].

In the as-built condition, AM parts are typically characterized by textured tracks related to the scanning strategy [16]. Because of really high cooling rates, their microstructure shows very fine columnar dendrites and cell structures whose morphology and size strongly depend on process parameters. Further modifications can be induced by partial re-melting induced by layers deposition [9, 17]. Because of the undercooling effect, inter-dendritic microstructure and chemical composition are generally really different from the center-dendrite ones [18]. From the point of view of fatigue resistance, the surface condition is the major critical aspect in AM components because of a normally high roughness and defects content in the near-surface layer. This peculiarity appreciably affects fatigue limits. Poulin et al. [4, 19] observed a detrimental reduction of fatigue strength with increasing porosity. In particular, axial fatigue tests with load ratio, $R = 0.1$, were performed. They observed fatigue limits of 590 MPa, 310 MPa, 220 MPa and 180 MPa with porosity levels of <0.1%, 0.3%, 0.9% and 2.7%, respectively. These results confirm the detrimental influence of defects on fatigue limits. For instance, in the worst condition (2.7% porosity fraction), the fatigue limit is reduced of approximately 70%. Then, Poulin et al. [4, 19] also studied the influence of porosity fraction on static tensile properties. They observed a negligible influence on the yield strength, while the ultimate tensile strength remained constant up to 0.3% porosity level and then it decreased. In particular, with the porosity levels of 0.9% and 2.7%, the UTS was reduced of 13% and 22%, respectively.

The high-cycle-fatigue performance of AM Inconel 625 has been investigated by several authors [8, 20–22], but much less information is available about the low cycle behavior. Pereira et al. [20] reported a fatigue limit in the AM condition of 244 MPa, whereas the conventional wrought material exhibited a fatigue limit of 550 MPa [21]. Poulin et al. [4, 19] investigated the influence of porosity on fatigue limits. They observed a fatigue limit ranging from 180 to 590 MPa with a porosity fraction varying from <0.1% to 2.7%.

As described, one of the most critical aspects of the SLM technique is the formation of process-induced defects which are mainly concentrated on the surface and in the near-surface regions [19, 23–26]. The presence of a poor surface quality dramatically affects the fatigue properties of components manufactured with this technique [19, 23, 25]. Many experimental works available in the literature focused on the influence of process parameters (laser power, scan speed, beam diameter) and powder characteristics on such detrimental features [23, 24, 26–28]. Joy Gockel et al. [26] concluded that increasing the laser power is beneficial for the surface roughness, but beyond a certain limit, keyholing occurs and sub-surface porosity is generated. Regarding the influence of the contour laser power, its increase determines an enlargement of the melted area resulting in re-melting of the previous layers. This reduces the amount of agglomerated powder stuck on the surface and it improves surface finishing [23]. These stuck and incrusted agglomerates are mainly generated because of the combination of two phenomena: contaminating liquid spatters and coalescence of un-melted powder located close to the melted walls [23]. Such particles, which are typically completely embedded in the surface layer, have a detrimental influence on the fatigue behavior. Regarding the influence of the contour scan speed and beam diameter, the surface roughness is increased with increasing the laser beam size [23]. At constant beam diameter, a reduction of the scan velocity is detrimental to surface roughness and porosity content. In fact, lower scan speeds promote turbulent melt pools and spattering on the built surfaces deteriorating surface finishing [23]. Typically, in the inner regions, porosities are few, small and with a low-roundness morphology. Instead, in the sub-surface layer, both defects size and roundness increase mainly because of the overlapping between the two strategies (external contour and inner hatching) [23]. In this case, another possible explanation is associated to the deceleration and acceleration of the scan head close to the contour. In fact, this promotes deeper melt pools and possible keyholing [23, 29].

Regarding the optimization and selection of the SLM process parameters, Letenneur et al. [30] developed a density prediction approach creating processing maps for Inconel 625 as a function of the layer thickness. A reduction of the layer thickness improves surface finishing and precision, but the process productivity is reduced [30]. For this reason, the authors recommended to work with layer thicknesses between 30 and 40 μm to enhance precision and between 50 and 60 μm to increase the build rate [30]. Once the layer thickness is selected, the processing maps allow to identify the correct combination of process parameters able to provide the desired densification [30]. Therefore, given the layer thickness (t), the processing maps allow to identify the optimal ranges for the melt pool size parameters: hatching space (h), melt pool depth (D) and width (W). This allows to

minimize the amount of porosities and improve the fatigue resistance. For Inconel 625, Letenneur et al. [30] obtained experimentally with a layer thickness of 40 μm that the optimal ranges (density $\rho > 99.5\%$) for the melt pool geometric characteristics are $1.5 \leq D/t \leq 2.75$, $1.8 \leq W/h \leq 2.8$ and $3.8 \leq L/w \leq 4.6$, where L is the melt pool length. Also, the powder characteristics have a great influence on the formation of defects. Regarding the powder morphology, for the same process parameters, adoption of powder with particles more spherical than elongated improves densification because of the enhanced powder flowability [27]. With the same process parameters, the variation of laser absorptivity of powder particles with different morphologies determines different spattering behaviors [24]. In particular, spherical powder particles reduce the spattering phenomenon [27].

Therefore, the process parameters and powder characteristics should be selected to minimize as much as possible the formation of defects. This is fundamental to improve the overall quality of a component in terms of fatigue behavior, especially.

According to Murakami [31, 32], defects can be converted into equivalent micro-notches and the corresponding fatigue limits can be determined by the Kitagawa–Takahashi approach [33, 34]. This procedure is often employed to justify that, after failure, the applied stress and the killer defect size exceeded the limit curve for fatigue resistance. Recently, a method was proposed to predict the fatigue limit based on the statistical analysis of defects observed by metallographic analysis [35]. In this case, the authors found a good agreement between predicted and experimental data.

According to the previous observations about optimization of process parameters, the content of defects can be minimized, but their presence cannot be avoided completely also because of process instabilities which are difficult to be controlled.

Therefore, the periodic control of the powder characteristics, porosities content and surface roughness are recommended during production to ensure consistent and reliable fatigue performance. Such features can be kept under control by destructive quality tests, like metallographic analyses, or non-destructive tests, like radiography and tomography, on some parts per batch and by roughness measurements. Since powder characteristics influence the porosity amount, size and morphology, high standards should be established to control the powder quality. Then, also the powder chemical composition should be controlled as well since metallurgical properties of components are strongly dependent on alloying elements.

Post-processing operations can be adopted to improve the surface quality of additively manufactured components to enhance their fatigue performance. These methods act removing or modifying the defects-rich surface layer. Chang et al. [36] summarized the most common surface modification techniques remarking their influence on the microstructure and the fatigue behavior. Particularly, great improvements can be obtained by HIP, laser shock and shot peening, as well as the use of advanced machining operations and chemical and electrochemical finishing. Mechanical treatments, such as shot peening, are appreciated also for the compressive state of stress induced on the surface and sub-surface zones.

Comparing AM and conventionally manufactured parts, one of the most important differences is the high production cost of the additive technique. This is acceptable only for components with high added value when the required geometrical features, static and dynamic properties, corrosion and high temperature resistance are almost impossible to be obtained with all the conventional casting and plastic deformation processes. As previously described, the most known and severe drawbacks are the presence of porosities, mainly located close to the surface, and the poor surface finishing which dramatically affects fatigue resistance. Such loss is generally not recovered by the high mechanical properties that often characterize AM parts. In fact, it is known that, when UTS increases, theoretical fatigue limits increase too. Nevertheless, sensitivity to notches and micro-notches increases as well. As a result, the practical fatigue limit undergoes a huge decrease. Moreover,
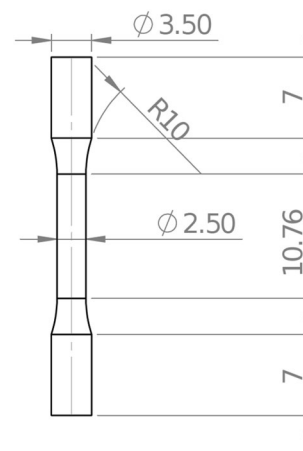

Fig. 1 Drawing of HCF and QS specimens adopted in this research work

Table 1 Chemical composition (wt. %) of the powder adopted in this work

	Ni (%)	Cr (%)	Mo (%)	Nb (%)	Fe (%)	Mn (%)	Si (%)
Inconel 625	61.5	21.2	9.55	4.05	2.80	0.05	0.02

even though it is generally true that fine microstructures improve fatigue resistance, the great improvement of static properties, especially yield strength, is not observed also for the fatigue properties when the characteristic microstructural dimension decreases below a certain limit. This was also observed in case of equiaxial grains obtained by severe plastic deformation [37]. Nor LCF, neither HCF properties result in improvements similar to those of the static ones, because the lower material deformability promotes early crack initiation.

In the present work, Inconel 625 was characterized by metallographic, hardness, micro-hardness and tensile tests. Then, also low-cycle-fatigue (LCF) and high-cycle-fatigue (HCF) tests were performed. The fatigue micro-mechanisms were studied by fracture surface SEM analysis. The high-cycle fatigue limit is generally determined by the stair-case method, as suggested by international standards [38]. As in this case, when the number of available specimens is limited, other methods have been studied and developed, such as the short stair-case approach [39–41]. Another method is the step loading technique [42]. In this case, given the initial stress level, the stress increment and the run-out cycles number, tests are performed at increasing stress levels until fracture [42]. The fatigue limit is determined by linear interpolation between the stress levels of the last not failed and the failed blocks, respectively. At the end, one or more confirmation tests are carried out at the calculated fatigue limit [42].

2 Materials and methods

The metal powder was supplied by SLM Solutions GmbH (Product 172015000568). Its chemical composition is reported in Table 1. The particle size of the powder was
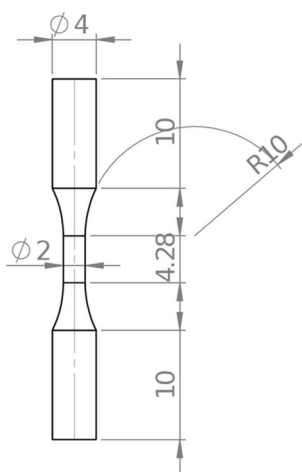
included between 10 and 45 μm and it was characterized by a spherical shape. The specimens adopted in this experimental work were printed using a EOS M 290 Metal 3D Printer and were tested in the as-built condition. Samples were manufactured in argon atmosphere using the following parameters: layer thickness of 40 μm, scan speed 900−1000 mm/s and power 300−400 W. The build direction corresponds to the longitudinal axis of each specimen, while the scanning direction lies on the transversal plane.

2.1 Surface roughness tests

In the as-built condition, because of its strong influence on fatigue crack nucleation, surface roughness was measured using a Taylor Hobson contact profilometer. According to EN ISO 21920-2:2022 standard [43], a selection of roughness parameters (R_a, R_t, R_z, R_v, R_c) was measured to characterize the surface completely.

2.2 Metallographic analysis

For all the tested materials, specimens in both the transversal and longitudinal directions were prepared by conventional metallographic procedure and analysed by light optical (LOM) and scanning electron (SEM) microscopy. In this case, a Leica (mod. DMR) light optical microscope and a Zeiss (mod. SIGMA 500) scanning electron microscope were adopted. The EDS detector (OXFORD Altee Energy—Advanced) available in the SEM was utilized to perform micro-chemical analyses. Specimens were mounted in cold-setting resin and mirror-polished. Etching was performed with a specific solution to reveal microstructural features. Using an image analysis tool, the porosity fraction and the area, roundness and distribution of defects were determined. The roundness parameter was defined considering Eq. 1.

$$\text{Roundness} = \frac{P^2}{4\pi A} \tag{1}$$

where A and P are the defect area and perimeter, respectively.

Fig. 2 Drawing of LCF specimens adopted in this work

Table 2 Roughness parameters measured on the investigated material

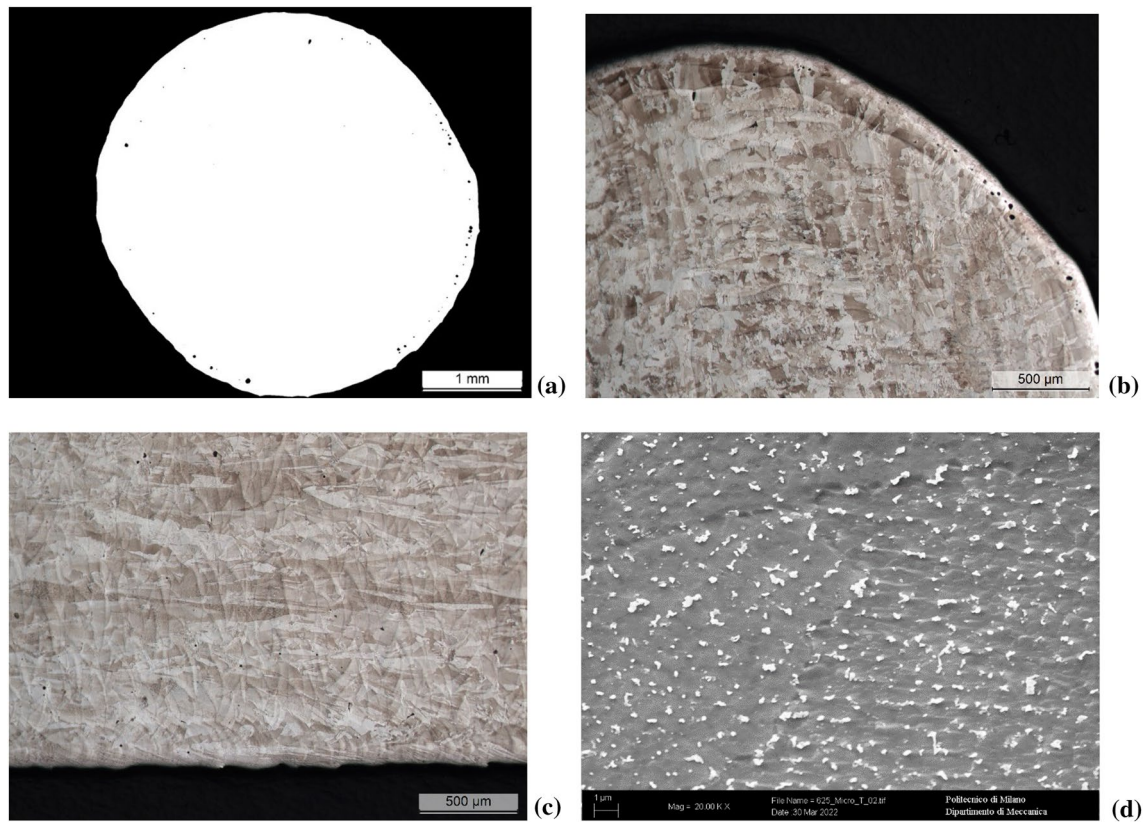|	Min [μm]	Max [μm]	Average [μm]
R_a	5.7	6.4	6.1
R_t	44.3	65.1	52.8
R_z	39.1	55.5	45.4
R_c	19.6	24.0	22.3
R_v	15.8	28.5	20.6

Fig. 3 Microstructure observed in the transversal **a**, **b** and longitudinal directions **c**. SEM image in the transversal plane **d**

2.3 Hardness, micro-hardness and tensile tests

Since additive manufacturing is completely different from conventional techniques, such as standard casting and plastic deformation, the resulting microstructures and mechanical properties cannot be easily foreseen. For this reason, mechanical tests are necessary to determine the elastic modulus, YS, UTS and the anisotropy in the building and the transversal directions. Hardness tests (HV2) were carried out on both the transversal and longitudinal sections. Moreover, micro-hardness profiles were performed starting from the outer surfaces to study possible hardness variations able to influence the fatigue limit. Vickers hardness tests (HV2 and HV0.1) were carried out using a Future Tech (mod. FM 700) hardness tester in accordance to the standard ISO 6507-1:2018 [44]. Then, room temperature tensile properties were determined by Quasi-Static (QS) tensile tests (crosshead speed equal to 0.1 mm/min). The tensile specimen geometry is equal to that adopted for HCF tests, as shown in Fig. 1. Tensile tests were performed using a STEPLab-UD04 machine (maximum load 5 kN).

2.4 High-cycle-fatigue (HCF) tests

As shown in Fig. 1, HCF tests with load ratio R = 0 were performed on cylindrical specimens using a STEPLab-UD04 machine (maximum load 5 kN and maximum frequency 35 Hz), according to ASTM E466 standard [45–47]. Considering the limited number of samples, the short stair-case statistical approach was adopted to determine the fatigue limits [39–41]. Tests were conducted considering different load levels. As in the standard stair-case approach, a force increment equal to 50 N was defined. Considering the
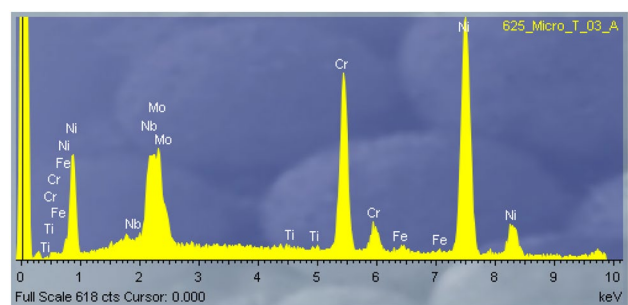

Fig. 4 EDS analysis of the precipitates shown in Fig. 3

specimen geometry, such force range corresponds to a stress interval equal to 10 MPa.

A first test is conducted at the starting force level, F_1. This value, which should be as close as possible to the fatigue limit, is estimated from literature. If the specimen withstands the run-out condition, 5×10^6 cycles, a subsequent test is performed at a force level increased by the force increment, i. e. $F_{i+1} = F_i + \Delta F$. Conversely, if the test ends with a failure, the following one is conducted at a force decreased by the force increment, i. e. $F_{i+1} = F_i - \Delta F$. Five tests were performed. In addition to the number of failures (X) and run-outs (O), their order is considered to determine the fatigue limit. The short stair-case method [48] determines the fatigue limit through a coefficient k, called Dixon factor, which is tabulated in [48]. Its value depends on the sequence of failures and run-outs. Equation 2 describes the calculation of the fatigue limit. x_F is the stress level of the last test.

$$\sigma_f = x_F + k\Delta\sigma. \tag{2}$$

2.5 Low-cycle-fatigue (LCF) tests

Low-cycle-fatigue (LCF) tests were performed on cylindrical specimens (Fig. 2) according to the standard ASTM E606 [49]. Because of the limited number of specimens, five samples were tested.

Tests were performed in strain control with strain ratio, R, equal to -1. The test frequency was set equal to the minimum value prescribed by the standard, i.e. 0.1 Hz [50]. This value was selected to prevent possible samples overheating that could affect the results.

2.6 Fracture surface observations

Selected broken fatigue specimens of both HCF and LCF tests were observed by SEM to determine the micro-mechanisms related to fatigue failure.

3 Experimental results

3.1 Surface roughness investigation

Five parameters were measured as summarized in Table 2. Data reported in Table 2 confirm the low surface quality.
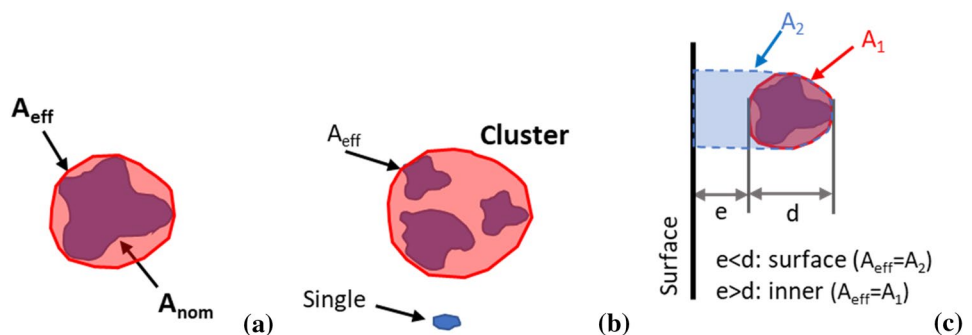
3.2 Metallographic investigation

Metallographic observations revealed a feature common to most of the AM parts, i.e. a large amount of micro- and macro-porosities mainly concentrated in a region close to the outer surface. Its radial width is about 180 μm. The percentage porosity was evaluated by image analysis in the transversal section on 25X magnification pictures. It resulted equal to about 0.2%. Porosity formation generally has two origins, one is metallurgical, i.e. the absorption of surrounding gases and/or the evaporation of alloying elements, and one is related to the un-melted zones, which depend on the building strategy [3, 51]. Melt pools are clearly visible in both transversal (Fig. 3a and b) and longitudinal directions (Fig. 3c). In the transversal direction, the elongated tracks of melt pools have different orientations, while in the longitudinal building direction, they show an almost uniform shape and orientation. The presence of a contour layer can be observed in both transversal and longitudinal planes [52]. In the outer layer, a large number of pores was observed too, mainly concentrated in

Table 3 Surface roughness, inner and surface defects observed in Inconel 625 specimens

Roughness Max R_v [μm]	Roughness micro-notch length [μm] (a)	Surface single and cluster defects (max) [μm] (b)	Micro-notch length (max) [μm] (c)	Inner single and cluster defects (max) [μm]
28.5	90	144	234	95

$(c) = (a) + (b)$

Fig. 5 Definition of the convex effective area of single defects **a** and cluster of defects **b** with and without presence of defect-surface interaction **c**. Classification and analysis according to the Murakami's method [31]
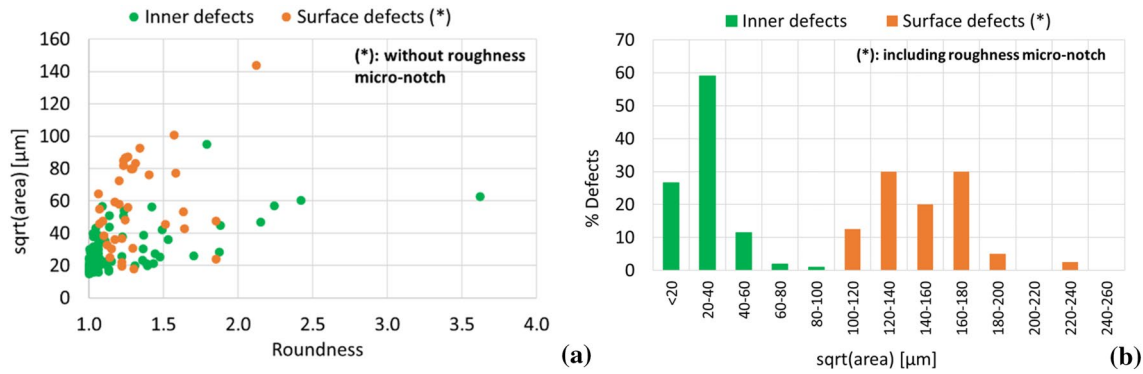
Fig. 6 Analysis of the observed defects – **a** Relation between roundness and equivalent micro-notch length, **b** distribution of inner and surface porosity
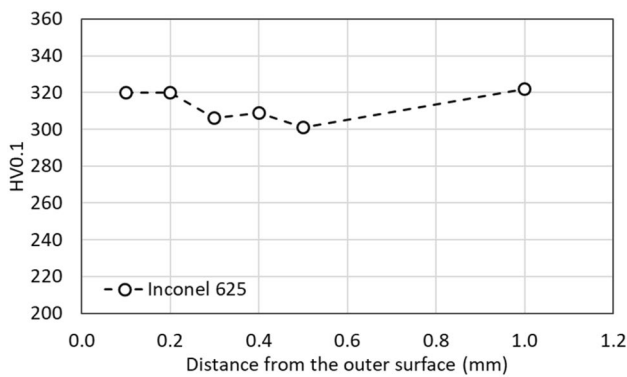

Fig. 7 Micro-hardness profile of the investigated alloy

Table 4 Tensile properties of the investigated material

YS [MPa]	UTS [MPa]	E [GPa]
630	827	210

the estimated P/v ratio for this work is equal to 0.393 J/mm. Considering the calculated scan speed of 932 mm/s, the estimated power results equal to 366 W which lies within the power range reported in the section Materials and methods. The volumetric laser energy density is given by $E = \frac{P}{vht}$ and, according to the calculated process parameters, it is equal to 89 J/mm^3. According to the literature data of Letenneur et al. [30], the minimum porosity content ($< 0.7\%$) is obtained with volumetric laser energy densities ranging from 53 to 116 J/mm^3. The energy density calculated for this work lies in the optimal range identified by Letenneur et al. [30] and it is also compatible with respect to the observed porosity content (0.2%).

SEM analysis revealed that the fine microstructure is characterized by presence of both cellular-shaped structures and elongated dendrites, whose growth is obtained in different orientations as function of the principal heat flux direction [52–57].

The microstructure observed by SEM is characterized by presence of high amount of Cr-Nb-Mo carbides, as confirmed by EDS analysis in Fig. 4. Their formation is induced by the high temperatures of the process, which promote segregation of low-melting elements in inter-dendritic spaces raising local concentrations of Nb, Mo and C. This condition can lead to the formation of precipitates composed of such alloying elements [52, 56].

Surface roughness and sub-surface defects are critical parameters to fatigue resistance. Assuming such defects as a single equivalent flaw, fracture mechanics principles are adopted to study fatigue life more deeply. Given the applied nominal stress σ, the Murakami's approach [31] suggests
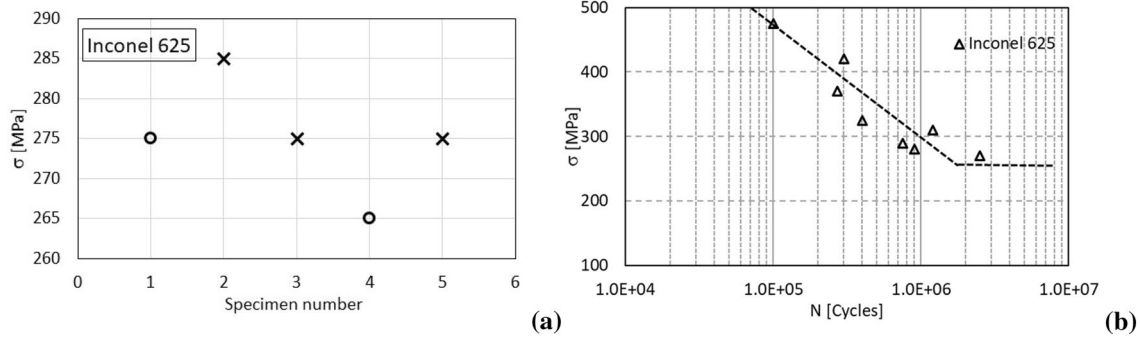
a sub-surface region, as shown in Fig. 3a. The melt pools are composed by a fine inner zone surrounded by coarser traces among adjacent pools. The geometry of the melt pools was measured on optical micrographs to analyse the dimensions of the hatch spacing, the melt pool depth and width. In particular, the average melt pool depth (D) is equal to 115 μm, the melt pool width (W) is 220 μm and the hatch spacing (h) is 110 μm. Considering the build rate (BR) recommended by the powder supplier (4.1 mm^3/s), it is possible to estimate the scan speed (v) having measured the layer thickness (t) and the hatch spacing (h). Being BR = vht, the estimated scan speed is equal to 932 mm/s and it lies within the scan speed range reported in the section Materials and methods. Approximating the melt pool area as half ellipse, its value is given by $A_{mp} = \frac{\pi D W}{4}$ and it is equal to 0.02 mm^2. Letenneur et al. [30] investigated the influence of power, scan speed and hatch spacing on density and melt pool depth and width for Inconel 625. Considering the literature data reported by Letenneur et al. [30], the relation between the power-to-scan speed ratio (P/v) and the melt pool area (A_{mp}) is given by: P/v[J/mm] $= 20.13 A_{mp}$[mm^2] $- 0.0074$. Therefore,

Fig. 8 Testing sequences **a** and Wöhler curve **b** of the investigated alloy

Fig. 9 Kitagawa–Takahashi diagram

Fig. 10 Comparison between the approaches of El-Haddad and Chapetti
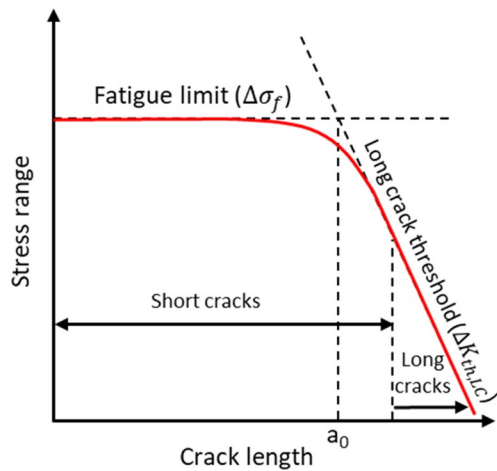
Eq. 3 to relate each defect to the applied stress-intensity factor K.

$$K = \sigma Y \sqrt{\pi \sqrt{\text{area}}}. \tag{3}$$

Y is equal to 0.65 and 0.50 for surface and internal defects, respectively. $\sqrt{\text{area}}$ is the effective length of the equivalent micro-notch calculated from the convex area of the defect determined according to the Murakami's method [31], as shown in Fig. 5a. This parameter is particularly important, since it is related to the shape, dimension and position of each defect. Since such defects are detrimental to fatigue resistance, they were deeply investigated considering classification into different classes, i. e. surface single, surface clusters, inner single and inner cluster defects. It is hence possible to define three possible crack nucleation promoters: surface roughness (case 1), near-surface single and cluster pores (considered surface defects) (case 2) and inner single and cluster pores (case 3). About case 2, the Murakami's theory [31] points out the difference among shallow or

deep defects (case 2.a) and all the others (case 2.b). About the conversion of the surface roughness into an equivalent micro-notch, the Murakami's approach was considered [31]. Being the roughness continuously distributed on the whole surface circumference, it was considered as a shallow defect with depth equal to the R_v parameter [58].

If only a single defect is present, the area is calculated as the convex contour which envelopes the original irregular shape, as shown in Fig. 5a. When multiple adjacent defects are present, interaction among them should be considered. A cluster is obtained when distances between adjacent defects are lower than the equivalent diameter of the smallest defect within the cluster, as shown in Fig. 5b. The cluster is characterized considering the convex area which circumscribes all the cluster-belonging defects. Then, the Murakami's approach considers the interaction of sub-surface defects with the surface [31]. When the distance from the surface (e) is higher than the defect size (d), the defect-surface interaction is negligible, as shown in Fig. 5c. Other authors [59] suggested to consider the $\sqrt{\text{area}}$ parameter instead of the defect size to assess the presence of defect–surface interaction.

Fig. 11 Definition of the crack length, the initial crack and the crack extension **a**; R-curve between the stress intensity range and the crack extension **b**
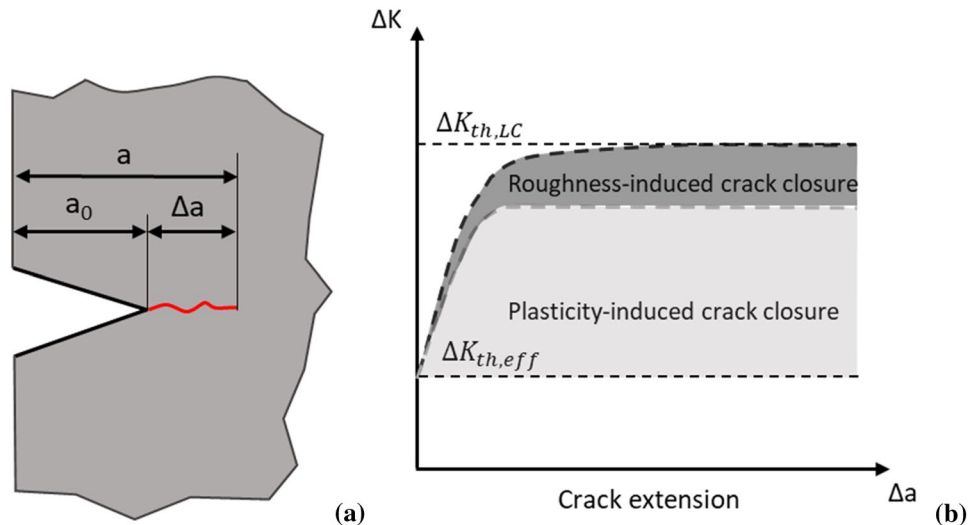
Regarding surface shallow defects, such as the surface roughness and surface defects with length-to-width ratio higher than 10, the effective length of the equivalent flaw is no longer calculated through the $\sqrt{\text{area}}$ size parameter, but considering the defect depth, t, as described by the Murakami's method [31]. Therefore, in this case, calculation of the stress-intensity factor is performed considering Eqs. 4 and 5.

$$K = \sigma Y \sqrt{\pi \sqrt{\text{area}_{\text{shallow}}}} \tag{4}$$

$$\sqrt{\text{area}_{\text{shallow}}} = \sqrt{10}t. \tag{5}$$

Therefore, inner and surface defects were classified according to the Murakami's theory [31]. They are reported in Table 3 together with the surface roughness conversion into the equivalent micro-notch. Since crack nucleation is generally driven by the worst defect, the maximum R_v parameter was selected to represent the notch effect of surface roughness [58]. The total length of each surface defect was obtained adding the length of the equivalent micro-notch to the roughness equivalent micro-notch. The defects detected by metallographic analysis were converted into equivalent micro-notches and classified according to their roundness and distribution, as shown in Fig. 6.

4 Hardness, micro-hardness and tensile tests

The hardness values in the transversal and the longitudinal sections are 273 HV2 and 303 HV2, respectively, remarking a slight hardness anisotropy. The micro-hardness profiles reported in Fig. 7 did not show substantial difference between outer and inner zones.

Regarding Inconel 625, Rivolta et al. [60–62] studied centrifugally cast rings for production of metallic gaskets and other forged components. They found average hardness values ranging from 80 to 90 HRB for the cast material and between 170 and 275 HV for the forged products characterized by grain size ranging from 230 to 18 μm. The previous data can be compared with those reported previously. The average hardness of the considered alloy is equal to 288 HV. This value is not only much higher than that of the centrifugal cast sample (according to ASTM E140-12b standard [63], 80 HRB–90 HRB can be converted to 151 HV–188 HV), but also higher than those of the fine-grained forged samples. The tensile properties are finally summarized in Table 4. Regarding the centrifugally cast alloy, Rivolta et al. [61] observed an yield strength ranging from 290 to 310 MPa and an ultimate tensile strength from 580 to 595 MPa. Regarding the forged products, Rivolta et al. [60, 62] found an yield strength from 315 to 460 MPa and an ultimate tensile strength from 750 to 910 MPa. The yield strength reported in Table 4 is significantly higher than that observed in both the centrifugally cast and fine-grained forged materials. Regarding the ultimate tensile strength, the additively manufactured alloy lies in the range of forged products, but it performs better than the centrifugally cast ring.

5 High-cycle-fatigue (HCF) tests

For the Inconel 625 alloy, the fatigue tests sequence was O-X-X-O-X, as reported in Fig. 8a. In this case, the Dixon factor is equal to − 0.305 leading to a fatigue limit of 272 MPa (with a 50% failure probability). In addition to

Table 5 Calculated $\Delta K_{th,eff}$ and $\Delta K_{th,LC}$ values for the investigated materials

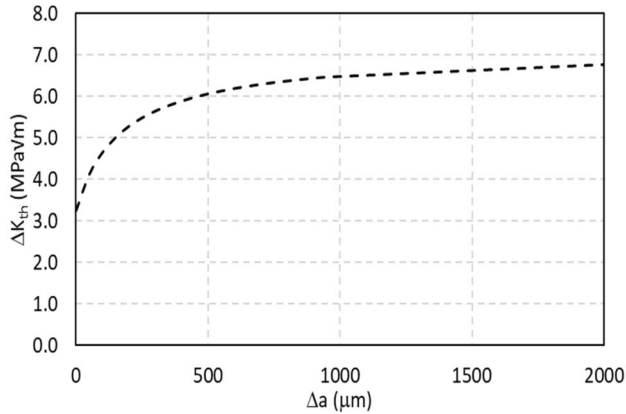| $\Delta K_{th,eff}[MPa\sqrt{m}]$	$\Delta K_{th,LC}[MPa\sqrt{m}]$
3.32	7.1

Fig. 12 Influence of crack length on the threshold ΔK

Table 6 Calculated theoretical fatigue limits ($R = 0$) and El-Haddad intrinsic cracks

$\sigma_{f0}[MPa]$	$a_0[\mu m]$
430	205

the fatigue limit zone, tests were conducted in the finite life region. The resulting Wöhler curve is shown in Fig. 8b.

Poulin et al. [22] studied the porosity influence on the fatigue limit of AM Inconel 625. Fatigue tests were performed with load ratio $R = 0.1$ and run-out condition equal to 10^7 cycles. When the porosity is equal to 0.3%, the obtained fatigue limit is similar (15% higher) to that found in this work.

5.1 Kitagawa–Takahashi (K-T) diagram and limit curves

The stress-intensity factor K defined in Eq. 4 can be adopted to study the fatigue behavior too. Particularly, El-Haddad et al. [64] suggested a relation between the threshold ΔK (ΔK_{th}) and the fatigue limit ($\Delta \sigma_f$) by defining an intrinsic crack, a_0, that considers the overall effect of existing defects. The relation among fatigue stress, threshold ΔK and crack length is summarized by the Kitagawa–Takahashi diagram [34] shown in Fig. 9.

The parameter a_0 defined by Eq. 6 represents the intrinsic crack related to the material microscopic features: microstructure, non-metallic inclusions, lattice defects, small cracks or damages induced by severe manufacturing
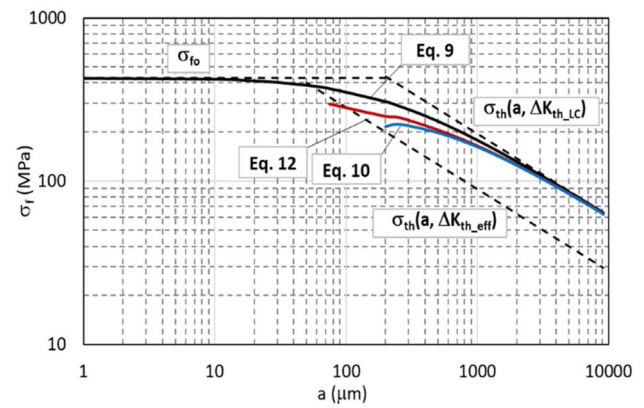
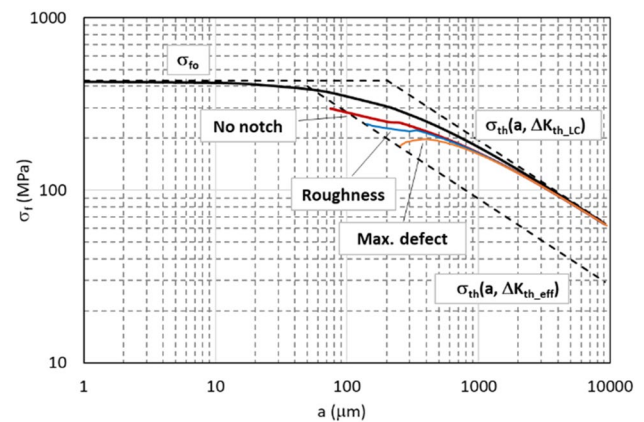**Fig. 13** Comparison among the limit curves for non-propagating cracks in the K-T diagram

Fig. 14 Comparison among the limit curves varying the initial micro-notch length

conditions, like large plastic deformation, or embrittlement phenomena, such as hydrogen embrittlement.

$$a_o = \frac{1}{\pi}\left(\frac{\Delta K_{th,LC}}{Y\Delta\sigma_f}\right)^2. \qquad (6)$$

$\Delta K_{th,LC}$ is the threshold ΔK for long cracks and $\Delta \sigma_f$ represents the fatigue limit.

However, in the case of cracks not associated to complete crack closure build-up, such as short cracks, the threshold ΔK can be reduced with respect to that of long cracks [65, 66]. Consequently, compared to the Chapetti's approach [67], the El-Haddad approximation is non-conservative, as shown in Fig. 10. Different methods were proposed to describe the crack closure build-up through exponential functions or other models which approach the long cracks ΔK_{th} threshold asymptotically [67–69]. Furthermore, investigating the effects of pre-existing flaws considered as sharp notches, Tanaka and Akiniwa [66]

demonstrated the reduction of the region of non-propagating cracks when the initial defect length increases. The R-curve was defined to relate the threshold stress intensity range to the crack length, as shown in Fig. 11.

The intrinsic (effective) threshold, $\Delta K_{th,eff}$, does not depend neither on the microstructure nor the load ratio, but only on material physical properties. The technical literature suggests different relations to determine its value. Li et al. [70] reported some prediction models mainly based on the elastic modulus, as shown in Eq. 7.

$$\Delta K_{th,eff} = \alpha \sqrt{|\boldsymbol{b}|} E, \tag{7}$$

where E is the elastic modulus, $\boldsymbol{b}$ is the Burgers vector and α is equal to 1 according to Hertzberg [71] or 0.75 according
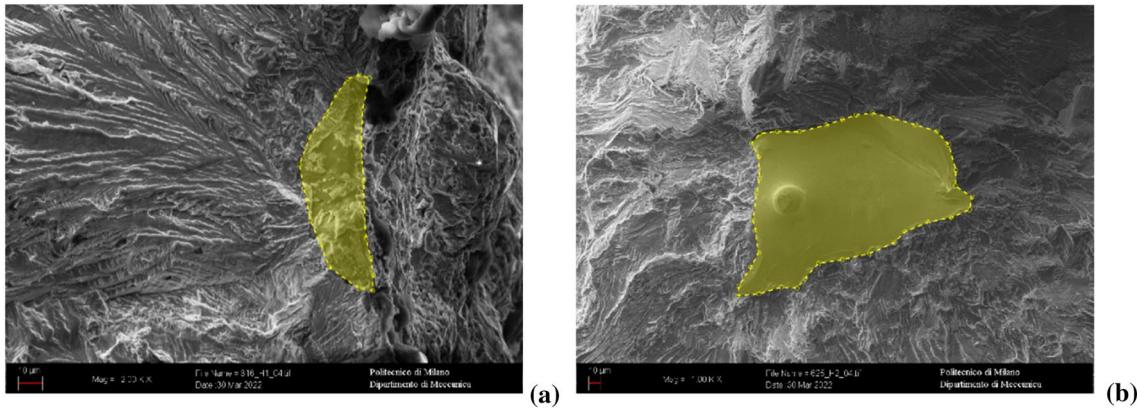
Fig. 15 Determination of the equivalent micro-notch length for surface and inner defects. **a** surface defect, **b** inner defect

Table 7 Summary of nucleation sites, total micro-notch lengths and fatigue stresses related to broken fatigue specimens

Nucleation site	Surface Roughness R_v [μm]	Micro-notch (roughness) [μm] (a)	$\sqrt{area}$ (defect) [μm] (b)	Micro-notch total length [μm] (c)	Fatigue stress [MPa]
Surface porosity	28.5	90	34	124	367
Inner porosity			136	136	326
Surface porosity			79	169	285

(a) Conversion of the roughness parameter R_v into the equivalent micro-notch length; (b) conversion of the observed defect into an equivalent micro-notch; (c) = (a) + (b)
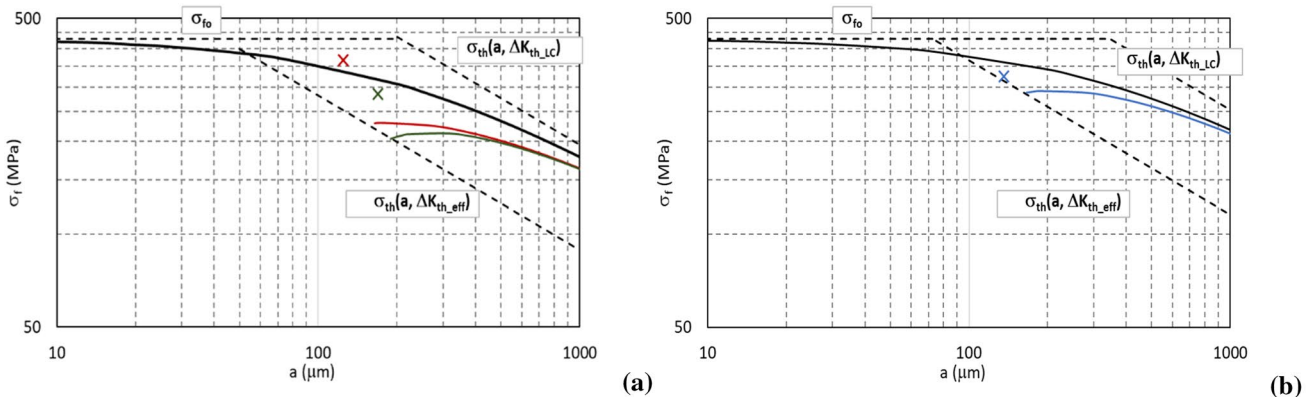

Fig. 16 K-T diagrams for the broken fatigue specimens summarized in Table 7. **a** Surface defects, **b** Inner defect
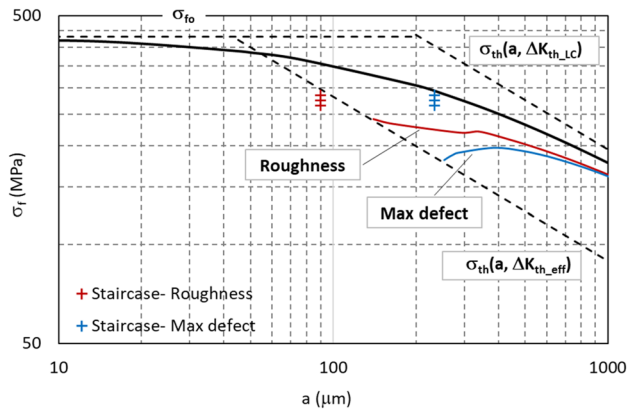
Fig. 17 K-T diagrams for the fatigue loads tested in the short stair-case tests
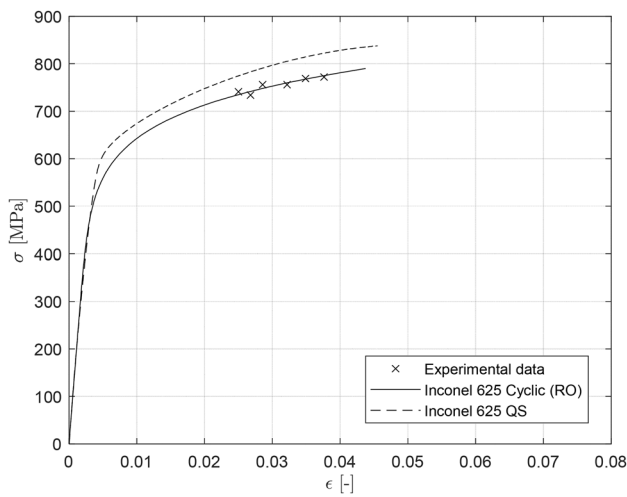

Fig. 18 Ramberg–Osgood cyclic curves compared to the quasi-static (QS) ones

to Pippan et al. [72]. The Burgers vector, defined by Eq. 8, is a function of the lattice parameters.

$$|\boldsymbol{b}| = \frac{a}{2}\sqrt{h^2 + k^2 + l^2}, \tag{8}$$

where a is the edge length of the unit cell, while h, k and l are the Burgers vector components. Since, in the FCC lattice, the family of directions $\langle 1, 1, 0 \rangle$ includes the most common sliding directions, $|\boldsymbol{b}| = \frac{a}{2}\sqrt{2}$.

As said previously, the El-Haddad limit curve described by Eq. 9 is non-conservative. As shown in Eq. 10, other authors suggested a slightly different expression considering the ΔK_{th} variation described by the R-curve [33, 67].

$$\Delta\sigma_{th} = \frac{\Delta K_{th,LC}}{Y\sqrt{\pi(a + a_o)}} \tag{9}$$

Table 8 Ramberg–Osgood parameters

K [MPa]	n [-]	E [MPa]
1141	0.1139	210,000

Table 9 Basquin-Coffin-Manson parameters

σ_f'[MPa]	b[-]	ε_f'[-]	c[-]
500	−0.050	0.077	−0.178

$$\Delta\sigma_{th} = \frac{\Delta K_{th}(a)}{Y\sqrt{\pi(a + a_o)}}. \tag{10}$$

The limit curve based on the intrinsic (effective) $\Delta K_{th,eff}$ threshold results in the non-propagating Chapetti region shown in Fig. 10. Replacing the El-Haddad parameter a_0 with a modified one, a_0', as reported in Eq. 11, a different form for the limit stress curve is obtained in Eq. 12.

$$a_o' = \frac{1}{\pi}\left(\frac{\Delta K_{th}(a)}{Y\Delta\sigma_f}\right)^2 \tag{11}$$

$$\Delta\sigma_{th} = \frac{\Delta K_{th}(a)}{Y\sqrt{\pi(a + a_o')}}. \tag{12}$$

Therefore, as discussed, the R-curves of the investigated alloys can be estimated considering different models at given $\Delta K_{th,eff}$ and $\Delta K_{th,LC}$ values. In this analysis, the authors adopted the model defined by Zerbst et al. [69] and reported in Eq. 13.

$$\Delta K_{th} = \Delta K_{th,LC}\sqrt{\frac{\Delta a + a^*}{\Delta a + a^* + a_o}}. \tag{13}$$

$\Delta K_{th,LC}$ is the threshold ΔK for long cracks, a_0 is the El-Haddad intrinsic crack and a^* is an additional parameter adopted to satisfy that $\Delta K_{th} = \Delta K_{th,eff}$ when $\Delta a = 0$. The a^* parameter is defined by Eq. 14.

$$a^* = a_o\frac{(\Delta K_{th,eff}/\Delta K_{th,LC})^2}{1 - (\Delta K_{th,eff}/\Delta K_{th,LC})^2}. \tag{14}$$

The intrinsic (effective) $\Delta K_{th,eff}$ threshold was determined averaging the values obtained with Eq. 7 considering the parameter α equal to 0.75 and 1 as suggested by Pippan and Hertzberg, respectively. The $\Delta K_{th,LC}$ threshold is strongly related to the microstructure and process parameters. For such reason, it was determined after a wide literature review. For Inconel 625, an average value of 7.1 MPa$\sqrt{\text{m}}$ was found [4, 25]. $\Delta K_{th,eff}$ and $\Delta K_{th,LC}$ values are summarized in Table 5. Then, the influence of crack length on the threshold ΔK is reported in Fig. 12.
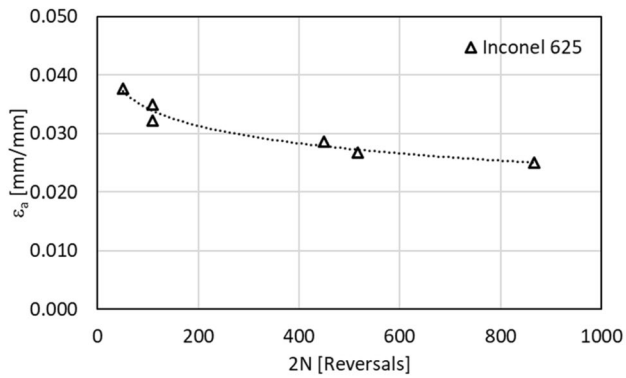
Fig. 19 Basquin-Coffin-Manson curve

The theoretical fatigue limit, σ_{f0}, is required to determine the K-T diagram. Its value can be estimated as a fraction of UTS. The technical literature suggests that the average ratio between the axial alternate fatigue limit ($R = -1$) and UTS ranges from 0.40 to 0.45 for conventional materials. In the case of $R = 0$, using the Goodman relation, it can be converted in the range from 0.57 to 0.62. Nevertheless, AM microstructures are significantly different from those obtained by conventional production processes. For this reason, a wide literature review of SLMed specimens was carried out [22, 23, 55, 57, 58, 73–77]. This analysis revealed a ratio included in the range from 0.40 to 0.65 for $R = 0$. Compared to data about conventionally manufactured alloys, the presence of a wider range for AM specimens is justified by the higher number of defects that can influence the fatigue life. In this analysis, an average ratio of 0.52 was considered. The theoretical fatigue limit is reported in Table 6 together with the El-Haddad intrinsic crack.

The limit curves for non-propagating cracks calculated according to Eqs. 9, 10 and 12 are compared in Fig. 13.

In the following analysis, Eq. 12 is selected as the reference model for the limit curve of non-propagating cracks. As discussed previously, surface roughness and surface/inner defects can be converted into equivalent micro-notches considering the Murakami's approach [31]. Their length influences the limit curves as reported in Fig. 14.

Some of the broken fatigue specimens were analysed by SEM, as shown in Sect. 7. Most of the crack nucleations occurred at the surface because of the roughness notch effect or the combined effect of roughness and near-surface pores. Only in one case, the crack nucleated from one inner
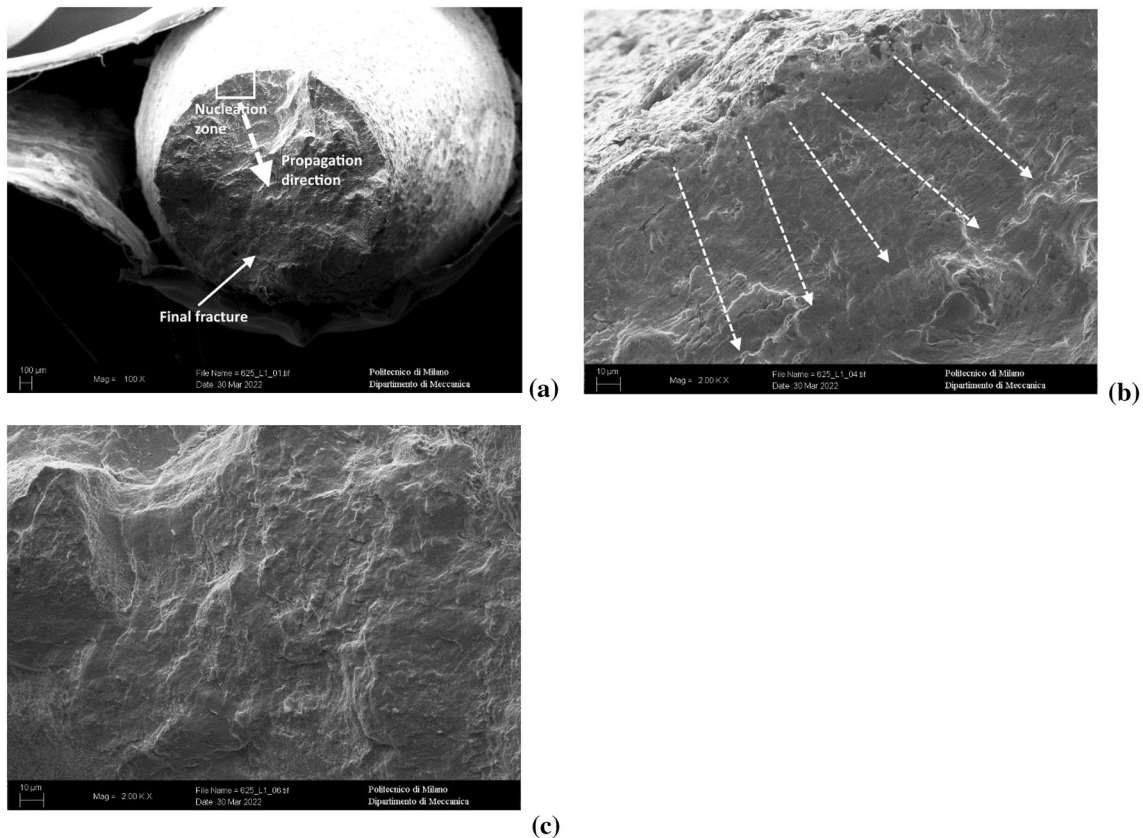

Fig. 20 Fracture surface analysis of specimen LCF1—**a** fracture surface, **b** nucleation zone, **c** propagation zone. No deeper investigation of the final fracture was possible because of damages occurred during specimen breakage
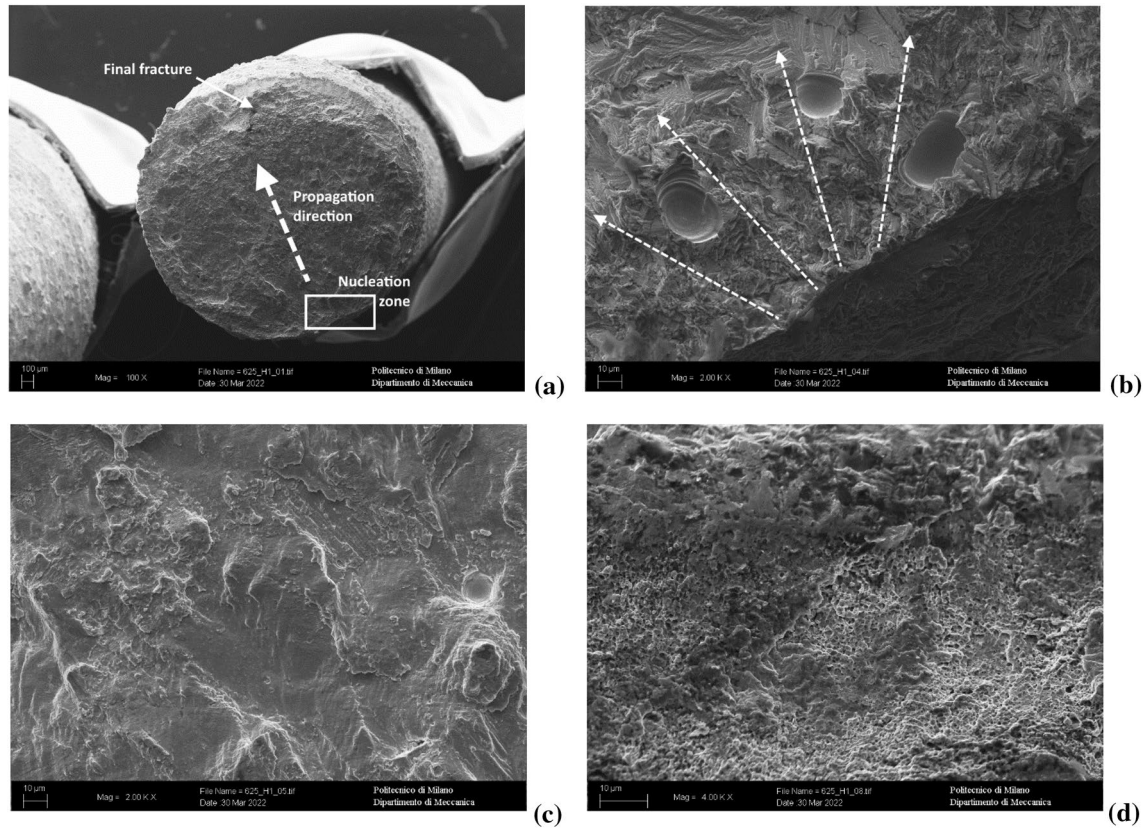
Fig. 21 Fracture surface analysis of specimen HCF1—**a** fracture surface, **b** nucleation zone, **c** propagation zone, **d** final fracture

porosity. According to the Murakami's approach [31], all the defects were converted into equivalent micro-notches. Considering the surface roughness as a shallow defect, its conversion into an equivalent micro-notch length can be calculated as $\sqrt{10R_v}$. For surface and inner defects, the same conversion is done considering the $\sqrt{area}$ parameter, as shown in Fig. 15. The equivalent micro-notch lengths are summarized in Table 7.

The broken fatigue specimens summarized in Table 7 were analysed using the K-T diagram referred to the corresponding material, as shown in Fig. 16.

All the broken fatigue specimens lie in the propagating crack region if compared to the corresponding limit curves. The El-Haddad limit curve is confirmed non-conservative since some of the broken fatigue samples fall into the safe zone. The stresses adopted for the fatigue tests, shown in Fig. 8, were reported on the related K-T diagram considering the minimum and maximum defect size. The minimum defect is represented by the surface roughness, whereas the maximum one is the largest observed by metallographic analysis. Since some samples survived and others failed, it is expected that only some conditions will fall in the K-T diagram safe zone. Such analysis is shown in Fig. 17.

6 Low-cycle-fatigue (LCF)

The tested material showed hysteresis curve. Interpolation of the stabilized cycles by the Ramberg–Osgood (RO) model reported in Eq. 15 is shown in Fig. 18.

$$\varepsilon_a = \varepsilon_{ae} + \varepsilon_{ap} = \frac{\sigma_a}{E} + \left(\frac{\sigma_a}{K}\right)^{\frac{1}{n}},\tag{15}$$

where ε_a is the total strain amplitude, ε_{ae} and ε_{ap} are the elastic and plastic portions of the total strain amplitude, σ_a is the stress amplitude, E is the elastic modulus, K and n are material constants. The RO parameters are reported in Table 8.

The stabilized curve shows a softening behavior. In general, when subjected to cyclic deformation over the elastic limit, materials undergo cyclic hardening or softening. Hardening occurs when the mechanical resistance is low, whereas softening is observed in high-strength materials. In order to better define the meaning of low and high mechanical properties, the technical literature [78] states that, when the monotonic strain-hardening exponent n, is higher than 0.15, cyclic strain hardening is expected, otherwise cyclic softening should occur. Cyclic hardening is related to the multiplication of dislocations induced by the applied strain
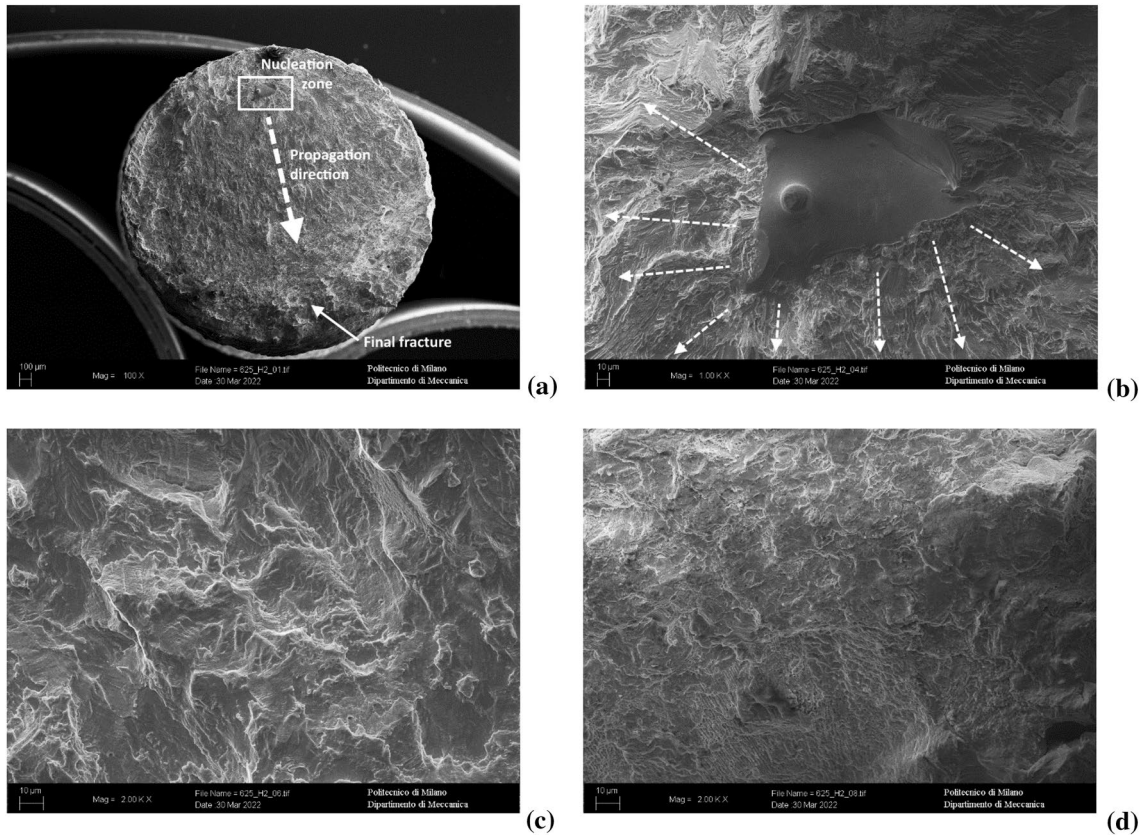
Fig. 22 Fracture surface analysis of specimen HCF2—**a** fracture surface, **b** nucleation zone (sub-surface nucleation), **c** propagation zone, **d** final fracture

Table 10 Specimens selected for SEM analysis of fracture surfaces and fatigue micro-mechanisms

Series	Code ID	Number of cycles to failure
Low cycle fatigue	LCF1	87
High cycle fatigue	HCF1	318,045
High cycle fatigue	HCF2	492,835

and to the high material deformability. The interaction of dislocations with themselves, with point defects and with grain boundaries cause the hardening effect. In AM components, the mechanical resistance is typically already high and the extremely fast solidification rates generate high dislocations and lattice defects densities [79, 80]. Therefore, in this case, cyclic softening is expected as a result of weakening and annihilation of obstacles to dislocations movements.

LCF tests were carried out until rupture and the number of cycles at failure, N_f, was recorded in each test. Then, the Basquin-Coffin-Manson (BCM) parameters (σ_f', b, ε_f', c) shown in Eq. 16 were determined.

$$\varepsilon_a = \frac{\Delta\varepsilon_a}{2} = \frac{\sigma_f'}{E}(2N_f)^b + \varepsilon_f'(2N_f)^c. \tag{16}$$

ε_f' is the fatigue ductility coefficient defined by the strain intercept at $2N_f = 1$. σ_f' is the fatigue strength coefficient defined by the stress intercept at $2N_f = 1$. $2N_f$ is the number of reversals to failure (N_f is the number of cycles to failure). b is the fatigue strength exponent and c is the fatigue ductility exponent. Their values are summarized in Table 9.

Then, Fig. 19 reports the obtained BCM curve.

7 Fracture surfaces

The analysis of the LCF fracture surfaces was really complicated because high loads reduce propagation areas. The investigated specimens are summarized in Table 10. In the LCF fatigue specimens, the typical fatigue marks are not as clear as those observed in the HCF ones. Moreover, some damages were observed on the fracture surfaces, which were probably generated when the final fracture occurred. Nevertheless, crack propagation evidences were detected

and highlighted in the SEM micrographs shown in Fig. 20. Instead, in the HCF series, nucleation, propagation and final fracture zones were clearer. In these specimens, most of the cracks originated on the outer surface and no multiple nucleation was observed. Only one specimen showed sub-surface crack nucleation, generated by an un-melted zone. For both LCF and HCF specimens, the final fracture is characterized by really small dimples associated with a micro-ductile mechanism as shown in Figs. 21 and 22. Inconel 625 is a FCC austenitic alloy with high deformability. This is confirmed by the micro-dimples observed on the fracture surfaces. Such high deformability allows to efficiently absorb the energy supplied during fatigue loading and this retards crack nucleation and propagation.

8 Conclusions

In this experimental study, Inconel 625 was produced, tested and characterized in terms of quasi-static, high-cycle-fatigue and low-cycle-fatigue. The mechanical resistance was determined by tensile and hardness tests resulting in better performance compared to conventional casting methods and sometimes even superior to wrought components. The SLM technique is very useful to generate complex geometries which are difficult to be obtained or cannot be generated with conventional manufacturing methods. This is especially important with reference to lattice structures and geometries improved by topological optimization softwares. However, critical aspects of this technique are the high costs and the low build rates which must be considered at the design stage. Moreover, as described throughout the paper, formation of defects still remains one of the major issues with a dramatic influence on the fatigue properties, especially. For this reason, as underlined in the paper, it is extremely important to embed quality control tests in the production system to monitor the amount, morphology, size and distribution of defects and ensure consistent, reliable and uniform components properties. Once the applied fatigue load is defined, this research work suggests a procedure to evaluate the position of a certain defect size with respect to the limit curve for non-propagating cracks. This tool can be embedded with quality control tests, such as X-ray tomography or metallographic analysis, to assess the compatibility of the maximum observed defect size with respect to the applied fatigue load. Despite the commonly poor fatigue properties of AM components, the static mechanical properties are generally higher than those obtained with conventional manufacturing techniques. This excellent feature of AM parts can be exploited to reduce component thicknesses, mass and so consumption of resources and carbon footprint. When fatigue resistance becomes important for a certain application, it is possible to adopt post-processing methods to improve the surface quality and reduce the content of defects in the near-surface layer. However, since some residual defects still remain, it is necessary to carefully control their amount and geometrical features to obtain a reliable prediction of the fatigue behavior based on the approach suggested in this paper.

Declarations

References

1. Sanaei N, Fatemi A (2021) Defects in additive manufactured metals and their effect on fatigue performance: a state-of-the-art review. Prog Mater Sci. https://doi.org/10.1016/j.pmatsci.2020.100724

2. Parizia S, Marchese G, Rashidi M, Lorusso M, Hryha E, Manfredi D, Biamino S (2020) Effect of heat treatment on microstructure and oxidation properties of Inconel 625 processed by LPBF. J Alloys Compd 846:156418. https://doi.org/10.1016/j.jallcom.2020.156418

3. Cao L, Li J, Hu J, Liu H, Wu Y, Zhou Q (2021) Optimization of surface roughness and dimensional accuracy in LPBF additive manufacturing. Opt Laser Technol 142:107246. https://doi.org/10.1016/j.optlastec.2021.107246

4. Poulin J-R, Kreitcberg A, Terriault P, Brailovski V (2019) Long fatigue crack propagation behavior of laser powder bed-fused Inconel 625 with intentionally-seeded porosity. Int J Fatigue 127:144–156. https://doi.org/10.1016/j.ijfatigue.2019.06.008

5. Neu RW, Sehitoglu H (1989) Thermomechanical fatigue, oxidation, and Creep: part II Life prediction. Metall Trans A 20:1769–1783. https://doi.org/10.1007/BF02663208

6. Neu RW, Sehitoglu H (1989) Thermomechanical fatigue, oxidation, and creep: part I. Damage mechanisms. Metall Trans A 20:1755–1767. https://doi.org/10.1007/BF02663207

7. Riccardo G, Rivolta B, Gorla C, Concli F (2021) Cyclic behavior and fatigue resistance of AISI H11 and AISI H13 tool steels. Eng Fail Anal 121:105096. https://doi.org/10.1016/j.engfailanal.2020.105096

8. Pratheesh Kumar S, Elangovan S, Mohanraj R, Ramakrishna JR (2021) A review on properties of Inconel 625 and Inconel 718 fabricated using direct energy deposition. Mater Today Proc 46:7892–7906. https://doi.org/10.1016/j.matpr.2021.02.566

9. Marchese G, Parizia S, Rashidi M, Saboori A, Manfredi D, Ugues D, Lombardi M, Hryha E, Biamino S (2020) The role of texturing and microstructure evolution on the tensile behavior of heat-treated Inconel 625 produced via laser powder bed fusion. Mater Sci Eng A 769:138500. https://doi.org/10.1016/j.msea.2019.138500

10. Suave LM, Cormier J, Villechaise P, Soula A, Hervier Z, Bertheau D, Laigo J (2014) Microstructural evolutions during thermal aging of alloy 625: impact of temperature and forming process. Metall Mater Trans A 45:2963–2982. https://doi.org/10.1007/s11661-014-2256-7

11. Floreen S, Fuchs GE, Yang WJ (1994) The metallurgy of alloy 625. In: Superalloys 718, 625, 706 and Derivatives, The Minerals, Metals & Materials Society, pp. 13–37

12. Sukumaran A, Gupta RK, Anil Kumar V (2017) Effect of heat treatment parameters on the microstructure and properties of Inconel-625 superalloy. J Mater Eng Perform 26:3048–3057. https://doi.org/10.1007/s11665-017-2774-8

13. Shankar V, Bhanu Sankara Rao K, Mannan SL (2001) Microstructure and mechanical properties of Inconel 625 superalloy. J Nucl Mater 288:222–232. https://doi.org/10.1016/S0022-3115(00)00723-6

14. Heubner U, Köhler M (1997) The effect of final heat treatment and chemical composition on sensitization, strength and thermal stability of alloy 625, In: Superalloys 718, 625, 706 and Derivatives, pp. 795–803

15. Yang L, Li Y, Chen Y, Yan C, Liu B, Shi Y (2022) Topologically optimized lattice structures with superior fatigue performance. Int J Fatigue 165:107188. https://doi.org/10.1016/j.ijfatigue.2022.107188

16. Hu Y, Lin X, Li Y, Ou Y, Gao X, Zhang Q, Li W, Huang W (2021) Microstructural evolution and anisotropic mechanical properties of Inconel 625 superalloy fabricated by directed energy deposition. J Alloys Compd 870:159426. https://doi.org/10.1016/j.jallcom.2021.159426

17. Sprengel M, Ulbricht A, Evans A, Kromm A, Sommer K, Werner T, Kelleher J, Bruno G, Kannengiesser T (2021) Towards the optimization of post-laser powder bed fusion stress-relieve treatments of stainless steel 316L. Metall Mater Trans A 52:5342–5356. https://doi.org/10.1007/s11661-021-06472-6

18. Arısoy YM, Criales LE, Özel T (2019) Modeling and simulation of thermal field and solidification in laser powder bed fusion of nickel alloy IN625. Opt Laser Technol 109:278–292. https://doi.org/10.1016/j.optlastec.2018.08.016

19. Poulin JR, Kreitcberg A, Terriault P, Brailovski V (2020) Fatigue strength prediction of laser powder bed fusion processed Inconel 625 specimens with intentionally-seeded porosity: feasibility study. Int J Fatigue. https://doi.org/10.1016/j.ijfatigue.2019.105394

20. Pereira FGL, Lourenço JM, do Nascimento RM, Castro NA (2018) Fracture behavior and fatigue performance of Inconel 625. Mater Res. https://doi.org/10.1590/1980-5373-mr-2017-1089

21. Kim K-S, Kang T-H, Kassner ME, Son K-T, Lee K-A (2020) High-temperature tensile and high cycle fatigue properties of Inconel 625 alloy manufactured by laser powder bed fusion. Addit Manuf 35:101377. https://doi.org/10.1016/j.addma.2020.101377

22. Poulin J-R, Kreitcberg A, Terriault P, Brailovski V (2020) Fatigue strength prediction of laser powder bed fusion processed Inconel 625 specimens with intentionally-seeded porosity: feasibility study. Int J Fatigue 132:105394. https://doi.org/10.1016/j.ijfatigue.2019.105394

23. Koutiri I, Pessard E, Peyre P, Amlou O, De Terris T (2018) Influence of SLM process parameters on the surface finish, porosity rate and fatigue behavior of as-built Inconel 625 parts. J Mater Process Technol 255:536–546. https://doi.org/10.1016/j.jmatprotec.2017.12.043

24. Yang G, Xie Y, Zhao S, Qin L, Wang X, Wu B (2022) Quality control: internal defects formation mechanism of selective laser melting based on laser-powder-melt pool interaction: a review. Chin J Mech Eng Addit Manuf Front 1:100037. https://doi.org/10.1016/j.cjmeam.2022.100037

25. Poulin J-R, Brailovski V, Terriault P (2018) Long fatigue crack propagation behavior of Inconel 625 processed by laser powder bed fusion: influence of build orientation and post-processing conditions. Int J Fatigue 116:634–647. https://doi.org/10.1016/j.ijfatigue.2018.07.008

26. Gockel J, Sheridan L, Koerper B, Whip B (2019) The influence of additive manufacturing processing parameters on surface roughness and fatigue life. Int J Fatigue 124:380–388. https://doi.org/10.1016/j.ijfatigue.2019.03.025

27. Tonelli L, Liverani E, Valli G, Fortunato A, Ceschini L (2020) Effects of powders and process parameters on density and hardness of A357 aluminum alloy fabricated by selective laser melting. Int J Adv Manuf Technol 106:371–383. https://doi.org/10.1007/s00170-019-04641-x

28. Scipioni Bertoli U, Guss G, Wu S, Matthews MJ, Schoenung JM (2017) In-situ characterization of laser-powder interaction and cooling rates through high-speed imaging of powder bed fusion additive manufacturing. Mater Des 135:385–396. https://doi.org/10.1016/j.matdes.2017.09.044

29. Sames WJ, List FA, Pannala S, Dehoff RR, Babu SS (2016) The metallurgy and processing science of metal additive manufacturing. Int Mater Rev 61:315–360. https://doi.org/10.1080/09506608.2015.1116649

30. Letenneur M, Kreitcberg A, Brailovski V (2019) Optimization of laser powder bed fusion processing using a combination of melt pool modeling and design of experiment approaches: density control. J Manuf Mater Process 3:21. https://doi.org/10.3390/jmmp3010021

31. Murakami Y (2002) Metal Fatigue, Elsevier, https://doi.org/10.1016/B978-0-08-044064-4.X5000-2

32. Masuo H, Tanaka Y, Morokoshi S, Yagura H, Uchida T, Yamamoto Y, Murakami Y (2017) Effects of Defects, Surface Roughness and HIP on Fatigue Strength of Ti-6Al-4V manufactured by Additive Manufacturing, In: Procedia Structural Integrity, Elsevier B.V., pp. 19–26. https://doi.org/10.1016/j.prostr.2017.11.055

33. Maierhofer J, Gänser H-P, Pippan R (2015) Modified Kitagawa-Takahashi diagram accounting for finite notch depths. Int J Fatigue 70:503–509. https://doi.org/10.1016/j.ijfatigue.2014.07.007

34. Kitagawa H (1976) Applicability of fracture mechanics to very small cracks or the cracks in the early stage, In: 2nd ICM, Cleveland, pp. 627–631

35. Rivolta B, Gerosa R, Panzeri D (2023) Selective laser melted 316L stainless steel: influence of surface and inner defects on fatigue behavior. Int J Fatigue. https://doi.org/10.1016/j.ijfatigue.2023.107664

36. Ye C, Zhang C, Zhao J, Dong Y (2021) Effects of post-processing on the surface finish, porosity, residual stresses, and fatigue performance of additive manufactured metals: a review. J Mater Eng Perform 30:6407–6425. https://doi.org/10.1007/s11665-021-06021-7

37. Estrin Y, Vinogradov A (2010) Fatigue behaviour of light alloys with ultrafine grain structure produced by severe plastic deformation: an overview. Int J Fatigue 32:898–907. https://doi.org/10.1016/j.ijfatigue.2009.06.022

38. BSI Standards Publication (2012) BS ISO 12107:2012: metallic materials — Fatigue testing — Statistical planning and analysis of data, BSI

39. Gorla C, Rosa F, Conrado E, Concli F (2017) Bending fatigue strength of case carburized and nitrided gear steels for aeronautical applications. Int J Appl Eng Res 12:11306–11322

40. Gorla C, Conrado E, Rosa F, Concli F (2018) Contact and bending fatigue behaviour of austempered ductile iron gears. Proc Inst Mech Eng C J Mech Eng Sci 232:998–1008. https://doi.org/10.1177/0954406217695846

41. Concli F (2018) Austempered ductile iron (ADI) for gears: contact and bending fatigue behavior. Procedia Struct Integr 8:14–23. https://doi.org/10.1016/j.prostr.2017.12.003

42. Bellows R (1999) Validation of the step test method for generating Haigh diagrams for Ti–6Al–4V. Int J Fatigue 21:687–697. https://doi.org/10.1016/S0142-1123(99)00032-8

43. BSI Standards (2022) ISO 21920–2:2022: geometrical product specifications (GPS) — Surface texture: Profile - Part 2: Terms, definitions and surface texture parameters

44. BSI Standards (2018) ISO 6507–1:2018: metallic materials – Vickers hardness test

45. Concli F, Fraccaroli L, Nalli F, Cortese L (2022) High and low-cycle-fatigue properties of 17–4 PH manufactured via selective laser melting in as-built, machined and hipped conditions. Prog Addit Manuf 7:99–109. https://doi.org/10.1007/s40964-021-00217-y

46. Maccioni L, Fraccaroli L, Borgianni Y, Concli F (2021) High-cycle-fatigue characterization of an additive manufacturing 17–4 PH stainless steel. Key Eng Mater 877:49–54. https://doi.org/10.4028/www.scientific.net/KEM.877.49

47. ASTM International (2021) E466 - 21: standard practice for conducting force controlled constant amplitude axial fatigue tests of metallic materials

48. Dixon WJ (1965) The up-and-down method for small samples. J Am Stat Assoc 60:967–978. https://doi.org/10.1080/01621459.1965.10480843

49. ASTM International (2021) E606/E606M − 21: Standard test method for strain-controlled fatigue testing, https://doi.org/10.1520/E0606_E0606M-21

50. Maccioni L, Rampazzo E, Nalli F, Borgianni Y, Concli F (2021) Low-cycle-fatigue properties of a 17–4 PH stainless steel manufactured via selective laser melting. Key Eng Mater 877:55–60. https://doi.org/10.4028/www.scientific.net/KEM.877.55

51. Cao Q, Bai Y, Zhang J, Shi Z, Fuh JYH, Wang H (2020) Removability of 316L stainless steel cone and block support structures fabricated by selective laser melting (SLM). Mater Des 191:108691. https://doi.org/10.1016/j.matdes.2020.108691

52. Nguejio J, Szmytka F, Hallais S, Tanguy A, Nardone S, Godino Martinez M (2019) Comparison of microstructure features and mechanical properties for additive manufactured and wrought nickel alloys 625. Mater Sci Eng A 764:138214. https://doi.org/10.1016/j.msea.2019.138214

53. Tridello A, Fiocchi J, Biffi CA, Rossetto M, Tuissi A, Paolino DS (2022) Size-effects affecting the fatigue response up to 109 cycles (VHCF) of SLM AlSi10Mg specimens produced in horizontal and vertical directions. Int J Fatigue 160:106825. https://doi.org/10.1016/j.ijfatigue.2022.106825

54. Tridello A, Fiocchi J, Biffi CA, Chiandussi G, Rossetto M, Tuissi A, Paolino DS (2020) Effect of microstructure, residual stresses and building orientation on the fatigue response up to 109 cycles of an SLM AlSi10Mg alloy. Int J Fatigue 137:105659. https://doi.org/10.1016/j.ijfatigue.2020.105659

55. Uzan NE, Shneck R, Yeheskel O, Frage N (2017) Fatigue of AlSi10Mg specimens fabricated by additive manufacturing selective laser melting (AM-SLM). Mater Sci Eng A 704:229–237. https://doi.org/10.1016/j.msea.2017.08.027

56. Silva CC, de Albuquerque VHC, Miná EM, Moura EP, Tavares JMRS (2018) Mechanical properties and microstructural characterization of aged nickel-based alloy 625 weld metal. Metall and Mater Trans A 49:1653–1673. https://doi.org/10.1007/s11661-018-4526-2

57. Bagherifard S, Beretta N, Monti S, Riccio M, Bandini M, Guagliano M (2018) On the fatigue strength enhancement of additive manufactured AlSi10Mg parts by mechanical and thermal post-processing. Mater Des 145:28–41. https://doi.org/10.1016/j.matdes.2018.02.055

58. Beretta S, Gargourimotlagh M, Foletti S, du Plessis A, Riccio M (2020) Fatigue strength assessment of "as built" AlSi10Mg manufactured by SLM with different build orientations. Int J Fatigue 139:105737. https://doi.org/10.1016/j.ijfatigue.2020.105737

59. Domfang Ngnekou JN, Nadot Y, Henaff G, Nicolai J, Kan WH, Cairney JM, Ridosz L (2019) Fatigue properties of AlSi10Mg produced by additive layer manufacturing. Int J Fatigue 119:160–172. https://doi.org/10.1016/j.ijfatigue.2018.09.029

60. Rivolta B, Gerosa R, Tavasci F, Ori Belometti L (2017) Mechanical and microstructural characterization of forged Inconel 625 ring gaskets for oil and gas application. Mater Perform Charact 6:20170030. https://doi.org/10.1520/MPC20170030

61. Rivolta B, Gerosa R, Tavasci F, Ori Belometti L (2017) Metallurgical analysis of Inconel 625 metallic gaskets produced by centrifugal casting. Mater Perform Charact 6:20170036. https://doi.org/10.1520/MPC20170036

62. Rivolta B, Boniardi MV, Gerosa R, Casaroli A, Panzeri D, Pizetta Zordão LH (2022) Alloy 625 forgings: thermo-metallurgical model of solution-annealing treatment. J Mater Eng Perform. https://doi.org/10.1007/s11665-022-07524-7

63. ASTM International (2012) E140 − 12b: Standard Hardness Conversion Tables for Metals Relationship Among Brinell Hardness, Vickers Hardness, Rockwell Hardness, Superficial Hardness, Knoop Hardness, Scleroscope Hardness, and Leeb Hardness, https://doi.org/10.1520/E0140-12B

64. El Haddad MH, Smith KN, Topper TH (1979) Fatigue crack propagation of short cracks. J Eng Mater Technol 101:42–46. https://doi.org/10.1115/1.3443647

65. Pippan R, Berger M, Stliwe HP (1987) The influence of crack length on fatigue crack growth in deep sharp notches. Metall Trans A 18:429–435

66. Tanaka K, Akiniwa Y (1988) Resistance-curve method for predicting propagation threshold of short fatigue cracks at notches. Eng Fract Mech 30:863–876. https://doi.org/10.1016/0013-7944(88)90146-4

67. Chapetti M (2003) Fatigue propagation threshold of short cracks under constant amplitude loading. Int J Fatigue 25:1319–1326. https://doi.org/10.1016/S0142-1123(03)00065-3

68. McEvily AJ, Minakawa K (1987) On crack closure and the notch size effect in fatigue. Eng Fract Mech 28:519–527. https://doi.org/10.1016/0013-7944(87)90049-X

69. Zerbst U, Madia M (2015) Fracture mechanics based assessment of the fatigue strength: approach for the determination of the initial crack size. Fatigue Fract Eng Mater Struct 38:1066–1075. https://doi.org/10.1111/ffe.12288

70. Li B, Rosa LG (2016) Prediction models of intrinsic fatigue threshold in metal alloys examined by experimental data. Int J Fatigue 82:616–623. https://doi.org/10.1016/j.ijfatigue.2015.09.018

71. Hertzberg RW (1995) On the calculation of closure-free fatigue crack propagation data in monolithic metal alloys. Mater Sci Eng A 190:25–32. https://doi.org/10.1016/0921-5093(94)09610-9

72. Pippan R, Riemelmoser FO (2003) Modeling of fatigue crack growth: dislocation models. Comprehensive structural integrity. Amsterdam, Elsevier, pp 191–207. https://doi.org/10.1016/B0-08-043749-4/04035-0

73. Riemer A, Leuders S, Thöne M, Richard HA, Tröster T, Niendorf T (2014) On the fatigue crack growth behavior in 316L stainless steel manufactured by selective laser melting. Eng Fract Mech 120:15–25. https://doi.org/10.1016/j.engfracmech.2014.03.008

74. Beretta S, Romano S (2017) A comparison of fatigue strength sensitivity to defects for materials manufactured by AM or traditional processes. Int J Fatigue 94:178–191. https://doi.org/10.1016/j.ijfatigue.2016.06.020

75. Spierings AB, Starr TL, Wegener K (2013) Fatigue performance of additive manufactured metallic parts. Rapid Prototyp J 19:88–94. https://doi.org/10.1108/13552541311302932

76. Beretta S, Patriarca L, Gargourimotlagh M, Hardaker A, Brackett D, Salimian M, Gumpinger J, Ghidini T (2022) A benchmark activity on the fatigue life assessment of AlSi10Mg components manufactured by L-PBF. Mater Des. https://doi.org/10.1016/j.matdes.2022.110713

77. Neu RW, Caputo AN, Gorgannejad S, Espejo Albela A, Carpenter MN, Zhang C, Tanna AH, Peloke B, Defay M, Collins JG, Sobotka JC, Popelar CF, Macha JH, Coogan SB (2022) Evaluation of HCF strength of Alloy 625 with non-optimum additive manufacturing process parameters. Int J Fatigue 162:106978. https://doi.org/10.1016/j.ijfatigue.2022.106978

78. Dieter GE (1988) Mechanical Metallurgy, McGraw-Hill

79. Wang G, Ouyang H, Fan C, Guo Q, Li Z, Yan W, Li Z (2020) The origin of high-density dislocations in additively manufactured metals. Mater Res Lett 8:283–290. https://doi.org/10.1080/21663831.2020.1751739

80. Hu D, Grilli N, Yan W (2023) Dislocation structures formation induced by thermal stress in additive manufacturing: multiscale crystal plasticity modeling of dislocation transport. J Mech Phys Solids 173:105235. https://doi.org/10.1016/j.jmps.2023.105235